Journal of Computational Physics 229 (2010) 1425–1447

Contents lists available at ScienceDirect

Journal of Computational Physics

journal homepage: www.elsevier.com/locate/jcp

Discretisation of diffusive fluxes on hybrid grids

G. Puigt [a,*], V. Auffray [b], J.-D. Müller [c]

[a] *CERFACS, European Center For Research and Advanced Training in Scientific Computations, 42 Avenue Coriolis, 31057 Toulouse Cedex 01, France*
[b] *ITK, 5 rue de la Cavalerie, 34000 Montpellier, France*
[c] *Queen Mary, University of London, Mile End Road, London E1 4NS, England, United Kingdom*

ARTICLE INFO

Article history:
Received 3 October 2008
Received in revised form 21 October 2009
Accepted 21 October 2009
Available online 10 November 2009

Keywords:
Finite volume
Hybrid mesh
Gradient reconstruction
Consistence
Stability

ABSTRACT

The main approaches of discretising the viscous operator of fluid flow on hybrid meshes are analysed for accuracy, consistence, monotonicity and sensitivity to mesh quality. As none of these approaches is fully satisfactory, a novel method using an approximated finite-element approach is presented and analysed. The methods are compared for the linear heat equation and the Navier–Stokes equations. While the novel approximated finite-element method performs significantly better for the linear heat equation, a stabilised edge-based method performs equally well for the considered test-cases for the Navier–Stokes equations.

1. Introduction

Unstructured tetrahedral meshes have become widespread in use for low and medium Reynolds number flow computations as complex geometries can be meshed with little effort. Many applications in CFD however involve the simulation of high Reynolds number flows with strong shear layers which are best captured on regular and aligned meshes. Typical are the use of hexahedral or prismatic elements in the boundary layer, which significantly increases the accuracy in the presence of very strong gradients normal to the wall. In addition, a hexahedral mesh has fewer elements and edges compared to a tetrahedral one with the same number of nodes. Hence a versatile CFD discretisation needs to be able to perform well on meshes composed of triangles and quadrilaterals in two dimensions, and tetrahedra, pyramids, prisms and hexahedra in three dimensions.

The typical mesh generation algorithms that are currently used add a few further requirements. While irregular meshes can be avoided by switching away from tetrahedra, a discretisation should be able to cope with skewed but regular meshes as often encountered, e.g. along curved boundaries or in turbo-machinery simulations. Hence accuracy should be maintained on parallelograms. High Reynolds number flows involve thin boundary layers which may require element aspect ratios in excess of 1000 for an efficient resolution and a discretisation has to be able to cope with that. The emerging unstructured quadrilateral and hexahedral mesh generation algorithms often produce meshes with irregular cells when coping with complex geometry. Hence a desirable aspect of the discretisation is to maintain accuracy on irregular quadrilaterals and hexahedra.

One can argue that the discretisation of the convective operator in the Navier–Stokes equations on hybrid grids is relatively straightforward, see e.g. Barth [1]. There is a degradation of the accuracy due to poor mesh quality on the one hand and

---

[*] Corresponding author. Tel.: +33 5 61 19 30 94; fax: +33 5 61 19 30 00.
E-mail address: guillaume.puigt@cerfacs.fr (G. Puigt).

0021-9991/$ - see front matter © 2009 Elsevier Inc. All rights reserved.
doi:10.1016/j.jcp.2009.10.037

due to loss of regularity at the hybrid interface on the other [2]. These effects are also present on purely triangular and in particular tetrahedral grids and typically can be dealt with through small amounts of mesh refinement.

On the other hand, the discretisation of the diffusive fluxes on hybrid grids is more difficult and no fully satisfactory approach has been presented to date. This paper seeks to analyse the possible variants for accuracy, consistence, monotonicity and sensitivity to mesh quality using Taylor analysis and positivity. The theoretical results are then tested by applying the best approaches to the linear heat equation and the Navier–Stokes equations.

In Section 2, the test problem is introduced, the discretisation of the convective fluxes is presented and the existing discretisation approaches for the diffusive fluxes are reviewed. Section 3 defines the geometry and recalls the commonly used extension of the convective discretisation to hybrid grids. Section 4 reviews the popular approaches for the discretisation of the viscous operator, while in Section 5 the formulation of four alternative discretisations for the diffusive operators are presented in detail and applied to the heat equation. Their consistence, accuracy, monotonicity and sensitivity to mesh quality is compared and verified in numerical tests. This study is performed using Taylor expansions and only local behaviour is of interest. This choice is motivated by the necessity to recover the desired accuracy on meshes composed of quadrilateral elements. Comparative results for the two useful discretisations for the Navier–Stokes equations are presented in Section 6, followed by concluding remarks in Section 7.

2. Problem description

To analyse the properties of the investigated discretisations, two model problems will be considered: the heat equation and the Reynolds Averaged Navier–Stokes (RANS) equations.

2.1. Heat equation

As a model problem for gradient reconstruction, let us consider the linear heat equation:

$$\frac{\partial T}{\partial t} = \alpha \Delta T, \tag{1}$$

where T is the temperature, α is the constant diffusive coefficient and Δ is the Laplacian. As we consider steady-state applications the derivative with respect to time t is not relevant. In a general framework, defining a control volume C with volume V, a finite-volume semi-discrete scheme can be expressed as:

$$V\left(\frac{\partial T}{\partial t}\right) = \alpha \int_{\partial C} \nabla T \cdot n\, ds, \tag{2}$$

where ∂C represents the boundary of volume C and n is the outward local unit vector, normal to ∂C.

2.2. Navier–Stokes equations

The compressible Navier–Stokes equations for air, which is assumed as a perfect gas, are written in the following compact conservative form (Eq. (3)):

$$\frac{\partial W}{\partial t} + \nabla \cdot F(W) = \nabla \cdot D(W, \nabla W), \tag{3}$$

where W represents the vector of conservative variables $(\rho, \rho U, \rho E)^T$ with the density ρ, the total energy E and the velocity vector U. $F(W)$ represents the convective operator and $D(W, \nabla W)$ represents the diffusive operator which depends on gradients of the variables. Introducing the pressure p and the total energy $E = e + 1/2\|U\|^2$ which is the sum of internal and kinetic energies, the Euler fluxes F and the viscous fluxes D are defined by:

$$F = [\rho U, \rho U \otimes U + pI, U(\rho E + p)]^T, \quad D = [0, \mathbf{S}, \mathbf{S} \cdot U - q]^T. \tag{4}$$

S is the stress tensor which becomes for a Newtonian fluid

$$\mathbf{S} = \mu\left(\nabla U + \nabla U^T - \frac{2}{3}\nabla \cdot U\mathbf{I}\right). \tag{5}$$

The molecular viscosity μ is a function of the temperature T through the Sutherland's law:

$$\mu = \mu_0 \left(\frac{T}{T_0}\right)^{\frac{3}{2}} \frac{T_0 + C_s}{T + C_s} \quad \text{with } C_s = 110.4\ \text{K}, \tag{6}$$

where μ_0 is the molecular viscosity at the reference temperature T_0. The heat flux q is modeled by the Fourier's law:

$$q = -\lambda \nabla T \quad \text{with } \lambda = \frac{C_p \mu}{Pr}, \tag{7}$$

where T is the temperature and λ is the thermal conductivity. The Prandtl number is $Pr = 0.72$ and C_p is the heat capacity at constant pressure. Finally, the equations are closed by the perfect gas law $p = \rho RT$ with $R = 287$ J/kg K.

Applying the standard finite-volume integration to Eq. (3) on a control element C with volume V, one finds

$$\frac{d}{dt}\int_C W\,dv + \int_{\partial C} F(W)\cdot n\,ds = \int_{\partial C} D(W,\nabla W)\cdot n\,ds, \tag{8}$$

with n being the unit outward normal to the dual volume boundary ∂C. The volume flux integrals have been converted to surface integrals using the Green–Gauss theorem.

3. Discretisation

Let $\{\tau_i,\ i = 1, N_\tau\}$ denote the N_τ elements of the mesh. These elements are triangles and quadrilaterals in two dimensions or tetrahedra, prisms, pyramids and hexahedra in three dimensions. From now on, this mesh will be called the 'primal' mesh and its elements will be denoted as the 'primitive' elements. In the vertex-centred finite-volume approach considered here, the flux balance is evaluated on a dual mesh composed of cells C_i around mesh nodes i.

3.1. Definition of dual cells for a hybrid mesh

The well-known extension of the definition of the median dual volume from simplex to primitive elements introduced by Dervieux [3] for the Euler equations and by Rostand and Stoufflet [4] for the Navier–Stokes equations is adopted here (Fig. 1). Hence, in two dimensions, the volume around a mesh node is limited by 'facets' linking the midpoints of the edges in the primal mesh to the barycentres of the elements obtained by arithmetic averaging of the nodal coordinates. In three dimensions, the dual volume is delimited by triangular facets between the edge midpoints, the face barycentres and the element barycentres.

3.2. Computation of convective fluxes

The extension of the convective flux computation to hybrid meshes is well-known, e.g. following [1], and reported here for completeness. For the Navier–Stokes equations, the convective fluxes F in Eq. (8) are computed with upwind schemes based on approximated Riemann solvers [5] at the dual interface. For the first-order convection scheme, the extension to hybrid meshes is straightforward since the only required quantities are the flow states W_i and W_j at the left and right hand sides of the interface, respectively, the edge-normal and the surface area. The edge-normal for a mesh edge ij is the sum of both facets attached to that edge as shown in Fig. 2.

Second-order accuracy is obtained by using a MUSCL-like extension [6–8] which involves a combination of upwind and centred gradients. More precisely, let ∇W_i be an approximation of the gradient of W at node i. For edge ij between nodes i and j, a second-order accurate convection scheme is obtained by replacing the states W_i and W_j by the states W_{ij} and W_{ji}, respectively. They are defined by:

$$\begin{cases} W_{ij} = W_i + 0.5\Phi(\beta\nabla W_i\cdot \vec{ij}, (1-\beta)(W_i - W_j)), \\ W_{ji} = W_j + 0.5\Phi(\beta\nabla W_j\cdot \vec{ij}, (1-\beta)(W_j - W_i)). \end{cases} \tag{9}$$

In Eq. (9), Φ is a slope limiter and computations were performed using a Van Albada-type limiter [9]. The positive constant β represents the amount of up-winding and is chosen here as $\beta = 2/3$. The gradient ∇W_i at node i is evaluated using Green–Gauss integration over the dual volume. Therefore, the same approach as in the simplex case in adopted and the numerical extension to hybrid grids does not present any particular difficulties. However, the weakness of the approach remains for non-simplex elements and for distorted cells, second-order of accuracy may be lost.

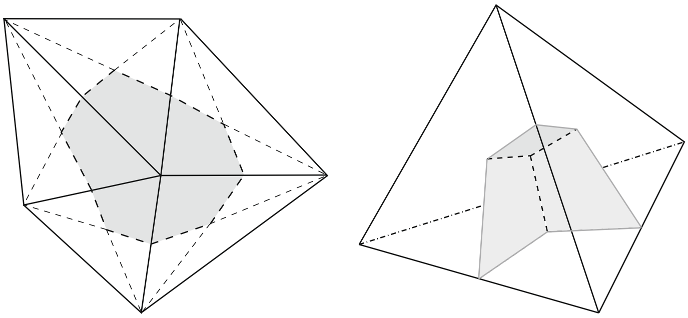

Fig. 1. Definition of the dual volume on a triangular mesh (left) and boundary of the dual volume inside a tetrahedron (right).

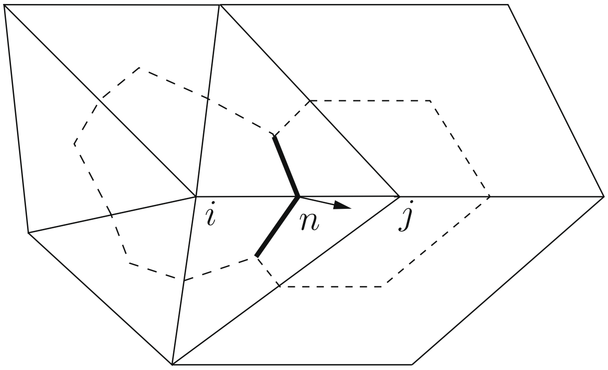

Fig. 2. Convection flux computation: definition of the surface and of the unit normal vector n for edge ij.

3.3. Computation of diffusive fluxes on simplices

On triangular and tetrahedral meshes, the standard P^1 finite-element discretisation induces a constant gradient over the element and a conservative scheme is built with the a "good" choice for diffusion coefficients. Moreover, following the definitions summarised in [10], a local analysis based on Taylor expansion shows that the P^1 finite-element discretisation is weakly consistent on any mesh composed of equilateral triangles. On the set of primitive mesh elements $E(i)$ containing node i, the diffusive term of Eq. (8) can be written as

$$\int_{\partial C_i} D(W, \nabla W) \cdot n \, ds = \sum_{T \in E(i)} \int_{\partial C_i \cap T} D(W, \nabla W) \cdot n \, ds. \tag{10}$$

The P^1 finite-element approach leads to a constant gradient on any simplex mesh element and for a diffusion term D which depends linearly of ∇W, the gradient can be factored out of the integral over $\partial C_i \cap T$. Billey et al. [11] demonstrated the equivalence of piecewise-constant finite-volume and P^1-Galerkin finite-element discretisation on a simplex mesh composed of triangles and Barth [1] gave a simple edge-based expression for the right hand side of Eq. (10).

However, the equivalence of these finite-volume and finite-element discretisations does not extend to non-simplex primitive elements. There is a range of possible discretisations for the viscous operator on hybrid grids with very distinct properties. An overview of existing methods is presented in the next section.

4. Computation of diffusive fluxes on non-simplex elements

A number of possible discretisations of the viscous terms on hybrid unstructured meshes have been presented in the literature.

4.1. "Edge-based" methods

Mavriplis and Venkatakrishnan [12] proposed an approach that consists of using the "thin shear layer" assumption in order to neglect cross-derivative terms, replacing the viscous term in the Navier–Stokes equations by the Laplacian. For a node i, this reduces the stencil to all the nodes j connected by an edge to node i and the diffusive flux balance on the dual cell can be split into edge contributions. This constitutes an advantage for the implementation in the popular edge-based framework [1,13] as contributions for convective and viscous fluxes can be computed in loops over edges only.

Haselbacher et al. [14] applied the edge-based discretisation of Mavriplis and Venkatakrishnan [12] to reconstruct the normal gradient component and a Green–Gauss formula to reconstruct the tangential gradient component. Numerical tests lead to the conclusion that the tangential component can be neglected without losing accuracy. This method is then equivalent to the "thin shear layer" assumption.

Instead of using the "thin shear layer" assumption, Galle [15] proposed to reconstruct the gradient at vertex i by a Green–Gauss formula applied on the dual cell C_i. The flux is then computed at mid-edge. He could show good agreement between computed and experimental results. Crumpton et al. [16] added a corrective term to the flux expression to improve stability on high aspect-ratio meshes. However, Eymard et al. [17] showed that this approach is second-order accurate only on a mesh composed of regular parallelograms. In conclusion, this approach is very simple and converges well but is only first-order accurate on irregular meshes.

4.2. "Cell-vertex" methods

In cell-vertex methods, a flux residual is computed over the primitive elements and is then distributed to each vertex using appropriate weights [18]. The stencil is compact and the scheme is linear preserving, i.e. second-order accurate. However, the scheme is not monotone on primitive elements and the use of an artificial viscosity model is required, which in turn reduces accuracy and may violate conservation.

Crumpton et al. [18] proposed three different gradient reconstructions defined in Fig. 3. The first one computes the NS and WE gradient components at node i (Fig. 3(a)). The reconstruction is simple but second-order accurate only on regular meshes. The second technique computes gradients on the primitive elements and interpolates the primitive element gradients to the mesh nodes (Fig. 3(b)). This approach is second-order accurate on meshes composed of parallelograms. Colin [19] showed that the scheme is not monotonic. Rudgyard [20] introduced a corrective term in the gradient expression to damp oscillatory chequer-board modes. The scheme is then monotonic but not conservative. Another variant of gradient reconstruction [21,22] consists of defining a control volume around each edge (diamond cell) and in applying a Green–Gauss formula (Fig. 3(c)). This method is shown to be inconsistent on stretched meshes [23].

Coirier [23] conducted an expansive and thorough study of the properties of discretisations of the viscous operator for regular, stretched and adaptive Cartesian meshes. In a cell-centred approach, he analysed the numerical behaviour of methods based on a Green–Gauss gradient reconstruction and methods based on a polynomial gradient reconstruction. The study revealed that the natural Green–Gauss reconstructions all lead to decoupled stencils which results in convergence problems.

Coirier also considered linear and quadratic reconstructions combined with a linear numerical scheme and found that the choice of the support volume is not straightforward. Only the quadratic approach reaches second-order accuracy but positivity is not guaranteed and the large required stencil leads to an ill-conditioned system for the polynomial coefficients. Studying in particular positivity and consistence, he concluded that it is impossible to define a general scheme for irregular meshes that is at the same time positive and consistent. He compared an accurate but not positive scheme to a positive but less accurate one. The study showed that both properties are important as they have a strong influence on convergence and stability.

Recently, Lipnikov et al. [24] proposed a new numerical scheme for general diffusion in two-dimension. Compared with Coirier's approach, the new scheme does not need any interpolation at mesh nodes and the numerical flux is more complicated. Actually, for each surface S between two cells C_i and C_j, the flux for a quantity U is a linear combination of contributions from cells C_i and C_j and the weights depend both on the cells geometry and on U, leading to a non-linear numerical scheme. Second-order of accuracy is guaranteed since the scheme is exact for linear and piecewise-linear solutions.

Despite the problems raised by Coirier about Green–Gauss gradient reconstruction, Khawaja [25] applied the Green–Gauss method to model turbulent flows on meshes composed of tetrahedra and prisms (subsonic flat plate, transonic flow over ONERA M6 wing, supersonic flow over HSTC aircraft, etc.). He obtained numerical results in close agreement with the experimental data.

Peroomian et al. [26] used a polynomial gradient reconstruction coupled with slope limiters to avoid oscillatory phenomena. The method does not seem to be completely satisfactory since slope limiters must be applied either to the conservative or to the primitive variables, depending the case.

4.3. Tessellation-like methods

A novel method for hybrid meshes was presented recently by Papin [27].

Papin uses the nodes of the primal mesh and the barycentres of faces and elements to define for each facet of the dual volume one specific triangle or tetrahedron, a "third mesh element", which contains that facet. As each third mesh element is a simplex, a constant gradient is defined using Green/Gauss integration or the equivalent standard P^1 finite-element approach. The proposed method is not a classical tessellation method since the facets of the dual volume are unchanged: the

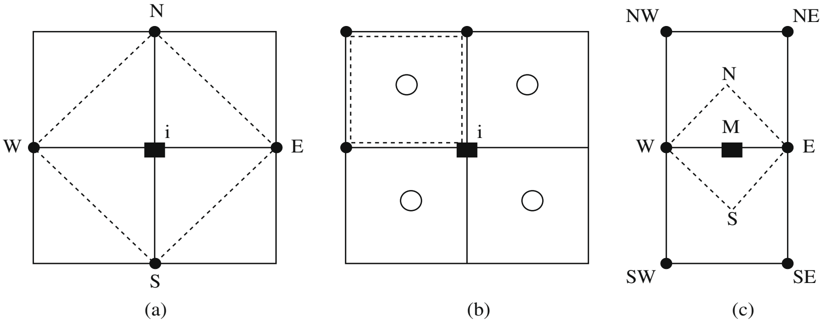

(a) (b) (c)

Fig. 3. Gradient reconstruction techniques (a) directly at node i, (b) from the element centroids and an interpolation, (c) edge-based approximation.

third mesh is only used to construct the gradient for the viscous flux computation. An example of a third mesh element used by Papin is given on Fig. 4.

The main interest of this technique is that the diffusive flux can be computed straightforwardly on this third mesh using the standard finite-element approach for simplex elements. Papin has shown that the third mesh elements can be obtained on any convex initial mesh. Second-order accuracy, conservation and consistence are obtained on regular parallelograms. Monotonicity is only obtained on rectangles. However, the scheme is computationally expensive since additional gradient evaluations are needed, such as in the barycentre of each element. Moreover, for meshes composed of elements with high aspect-ratio such as in a boundary layer, the third mesh elements can be of very poor quality.

4.4. "Discontinuous Galerkin" approach

Another kind of method is based on the Discontinuous Galerkin (DG) technique. The DG technique was first introduced by Reed and Hill in 1973 [28] for neutron transport and by Nitsche [29] in 1971 for the approximation of elliptic equations. Following the work of Cockburn and Shu [30] in 1989, several authors have worked on this technique for the last decades.

The DG method uses a piecewise polynomial data representation over the element that allows discontinuities at the cell interfaces. A DG method if limited to only piecewise-linear data and a second-order MUSCL finite-volume method [31] have the same data representation. However, while the MUSCL method reconstructs the gradients from the conservative flow field, the DG method solves a transport equation for the unknown cellwise gradient. Hence, as opposed to a piecewise-linear finite-element approach with a continuous reconstruction [1], a full DG diffusion scheme cannot be simply implemented within the context of a MUSCL-based finite-volume method, however, a finite-volume viscous flux approximation could take inspiration from the DG formulation of the viscous flux limited to P^1 elements only. The aim to achieve would be to exploit the discontinuous representation to arrive at an accurate and consistent flux formulation for steep gradients over very few mesh points, similarly to the resolution of shock waves with shock-capturing finite-volume schemes.

The DG discretisation of the diffusive flux is presented here for completeness and to stimulate further development, we do not aim to present an exhaustive discussion here. The reader is referred to the broad summary of Arnold et al. [32].

Zhang and Shu [33] use Fourier analysis to show that simple Taylor analysis as performed by the present authors can produce misleading results for DG discretisations of the diffusion equation.

As our aim is to develop a viscous approximation that can be used transparently with the existing popular MUSCL-based finite-volume discretisations, we focus on two approaches closest to the finite-volume method.

The approach presented by van Leer and Nomura [34] in 1D performs a smooth reconstruction at the cell interfaces. A particular choice of approximation to the interface terms based on physical reasoning leads to a conservative stabilisation term which is of $O(1/\Delta x)$ and which had not been presented in the unified formulation of Arnold et al. [32].

Gassner et al. [35] derive a solution for a diffusive generalised Riemann problem leading to a space–time formulation for the convection–diffusion equation. To achieve second-order accuracy within a finite-volume method a polynomial reconstruction of order 3 would be required, which does not easily fit within the framework of existing finite-volume MUSCL methods. Second-order accuracy can only be achieved within a DG framework that formulates an adjoint-consistent update equation for the gradient [35].

4.5. Summary

This overview demonstrated the difficulties in defining a numerical scheme for hybrid meshes that is consistent, conservative, sufficiently accurate, positive with a good convergence property and with a reasonable computational cost. In the next section, we shall analyse four of the most promising approaches and evaluate their performance for the heat equation.

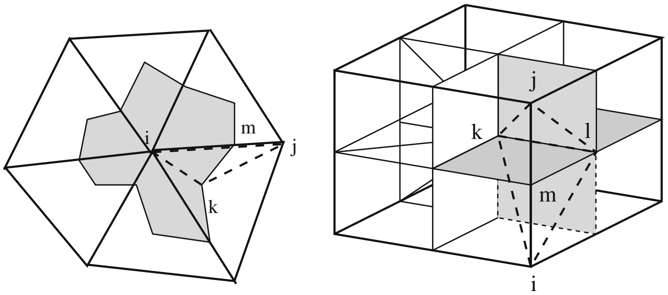

Fig. 4. Left hand side: triangle *ijk* is used for the computation of the flux on dual cell facet *mk*. Right hand side: tetrahedron *ijkl* is needed for the computation of the gradient for flux balance on facet *klm*.

5. Comparison of four discretisations for the diffusive operator and application to the heat equation

5.1. Notations

All explanations are based on the notations introduced in Fig. 5 in a two-dimensional context. In the following, let $N(i)$ be the set of nodes j that are linked to node i through the mesh edge ij and let $\tau(i)$ be the set of mesh elements τ formed with node i. The dual cells C_i and C_j around nodes i and j, respectively, share the interface $\partial C_{ij} = \partial C_i \cap \partial C_j$. The facets of the dual volume C_i around node i that lie within the primal mesh element τ are $\partial C_i \cap \tau$ and have the outward normal n_i^τ.

5.2. Necessary properties

An efficient numerical method should satisfy the following properties [1]:

(i) consistence,
(ii) conservation,
(iii) monotonicity,
(iv) second-order accuracy,
(v) insensitivity of precision and convergence to deterioration in mesh quality,
(vi) compact support.

Property (ii) is necessary to ensure a global mass conservation. Even if this point is not so clear for a perfect gas solver, conservation of the solver guarantees that mass fractions are bounded during the computation of multi-species flows with chemical reactions. A monotone discretisation (iii) ensures that the solution observes a maximum principle, which is required on the one hand for bounded fields in turbulence modelling and multi-species flows, and on the other hand for good stability and good convergence rates. Compact support (vi) is important for effective parallelisation and for resolution of the highest frequency modes.

Local analysis of consistence is conducted using Taylor analysis and monotonicity is analysed by a positivity argument [1]. These properties are analysed in the following for an edge-based discretisation, a cell-vertex discretisation the standard finite-element method and a novel approximated finite-element method based on nodal gradients.

5.3. The edge-based approach

As an example for an edge-based discretisation, we shall start from Galle's formulation [15]. The principle is to define a gradient at node i by integration over the dual cell boundary associated with node i, assuming linear variation of T along each edge:

$$\nabla T_i = \frac{1}{V_i} \iint_{\partial C_i} T n \, ds = \frac{1}{V_i} \sum_{j \in N(i)} \frac{T_i + T_j}{2} \iint_{\partial C_{ij}} n \, ds. \tag{11}$$

The gradient at ∂C_{ij} is then taken as the mean value of the gradient at nodes i and j:

$$\nabla T_{ij} = \frac{\nabla T_i + \nabla T_j}{2}. \tag{12}$$

Finally, the stability is improved with Crumpton's correction [16] for the interface gradient:

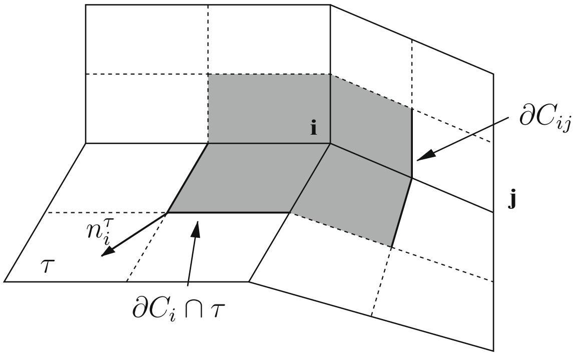

Fig. 5. Definition of sub-surfaces of the dual cell C_i around node i.

$$\nabla T_{ij}^{corr} = \nabla T_{ij} - \left(\nabla T_{ij} \cdot \delta_{ij} - \frac{T_j - T_i}{\|x_j - x_i\|}\right)\delta_{ij}, \tag{13}$$

with

$$\delta_{ij} = \frac{x_j - x_i}{\|x_j - x_i\|} \tag{14}$$

and $x_i,\ x_j$ representing the coordinates of vertex $i,\ j$, respectively.

Using Eqs. (12), (13) and the definition of δ_{ij} (Eq. (14)), the scheme is shown to be conservative. The discretisation is consistent, monotonic and second-order accurate on rectangular meshes only [36]. On regular parallelograms, the discretisation is consistent and second-order accurate.

A truncation error analysis on arbitrary quadrilaterals demonstrates a first-order error. Moreover, in this case, the method is neither consistent nor monotone. In the following, the method will be denoted "EB".

5.4. The cell-vertex approach

As an example of the cell-vertex approach, let us consider the approach proposed by Crumpton et al. [18], Fig. 3(b). Applying the Green–Gauss theorem, one obtains a constant gradient for each primal mesh element:

$$\nabla T^{\tau} = \frac{1}{V_i}\iint_{\partial\tau} Tn\,ds, \tag{15}$$

where τ is an element of the primal mesh. The diffusive flux at node i is then computed from:

$$\alpha\iint_{C_i} \nabla T \cdot n\,ds = \alpha \sum_{\tau\in\tau(i)} \nabla T^{\tau} \cdot n_i^{\tau}. \tag{16}$$

This formulation is easy to implement and is interesting because the cell gradient is also required for the computation of convective terms in cell-vertex methods [37], resulting in computational savings. Truncation error analysis shows that the numerical scheme is second-order accurate and consistent on meshes composed of parallelograms [36]. On meshes composed of other types of elements, consistence has not been demonstrated. However, the stability analysis reveals that the discretisation is not monotone and oscillatory solutions can develop. To avoid these spurious chequer-board modes, a correction similar to the one for the edge-based method (Eq. (13)) is added to the gradient expression [20]. The stabilised flux expression becomes:

$$\alpha\iint_{C_i} \nabla T \cdot n\,ds = \alpha \sum_{\tau\in\tau(i)} \nabla T_i^{\tau} \cdot n_i^{\tau}, \tag{17}$$

with the following gradient expression:

$$\nabla T_i^{\tau} = \nabla T^{\tau} - \delta_c\left(\nabla T^{\tau} \cdot \delta s_i - \frac{(T^{\tau} - T_i)}{\|x^{\tau} - x_i\|}\right) \cdot \delta s_i. \tag{18}$$

∇T^{τ} is defined by Eq. (15), δ_c is a modelling parameter, T^{τ} is the mean value of T on $\tau,\ x^{\tau}$ the centroid coordinates and δs_i is defined by:

$$\delta s_i = \frac{x^{\tau} - x_i}{\|x^{\tau} - x_i\|}. \tag{19}$$

This correction introduces a modification of the gradient in the direction of the "diagonal" of the element and this correction makes the formulation non-conservative.

A theoretical analysis that takes into account this correction (Eq. (18)) shows that the scheme is consistent on regular rectangular meshes only and that the discretisation is monotonic if the value for δ_c is chosen in an interval which depends on the mesh geometry [36]. In two dimensions and for a quadrilateral element denoted $ABCD$ with diagonals of length AC and BD and with area $\mathcal{A},\ \delta_c$ must satisfy:

$$\frac{|AB^2 - AC^2|AC^2}{2\mathcal{A}} < \delta_c < \frac{BD^2AC^2}{2\mathcal{A}}. \tag{20}$$

In the following, the method will be denoted "CV".

5.5. Finite-element reconstruction approach

As an alternative to both previous formulations, the P^1 finite-element method can be extended to primitive elements: the idea is to reconstruct the gradient using the finite-element basis functions of the specific element class. One of the advantages of this approach is that the method reverts to the P^1 formulation on simplex elements, which is popularly used.

The gradient at any point (x,y) of an element τ can be evaluated with the finite-element approach:

$$\nabla T(x,y)=\sum_{k\in S^\tau}T_k\nabla N_k^\tau(x,y), \tag{21}$$

where (x,y) are the coordinates of a point which belongs to element τ of the primal mesh. N_k^τ denotes the shape function of element τ associated with node k and S^τ is the set of nodes of τ. The gradient computation is therefore transferred to the evaluation of the shape function gradients. The computation of the shape function gradient is based on the transformation to iso-parametric coordinates.

As an example, one may consider in two dimensions the integration of the flux on $\partial C_A\cap\tau$ where C_A is the dual cell around node A and τ is the quadrilateral $ABCD$, as described on Fig. 6.

Using the Jacobian transformation J^τ from original (x,y) to iso-parametric (ξ,η) space, the numerical flux I becomes

$$I=\int_{\partial C_A\cap\tau}\alpha\nabla T\cdot n\,dl=\int_{\partial C_A\cap\tau}\alpha\left(\sum_{i=1}^{4}T_i\nabla_{xy}N_i^\tau\right)\cdot n\,dl=\int_{\partial C_A\cap\tau}\alpha\left(\sum_{i=1}^{4}T_i[J^\tau]^{-T}\nabla_{\xi\eta}N_i^\tau\right)\cdot n\,dl, \tag{22}$$

where J is the Jacobian matrix associated with the transformation from (x,y) space to (ξ,η) one. Using the transformation (Fig. 6), $n\,dl$ becomes:

$$n\,dl=\begin{pmatrix}-dy\\ dx\end{pmatrix}=\begin{pmatrix}-\frac{\partial y}{\partial\xi}(\xi,\eta)d\xi-\frac{\partial y}{\partial\eta}(\xi,\eta)d\eta\\ +\frac{\partial x}{\partial\xi}(\xi,\eta)d\xi+\frac{\partial x}{\partial\eta}(\xi,\eta)d\eta\end{pmatrix}. \tag{23}$$

Defining functions a and b by:

$$\sum_{i=1}^{4}T_i[J^\tau]^{-T}\nabla_{\xi\eta}N_i^\tau=\begin{pmatrix}a(\xi,\eta)\\ b(\xi,\eta)\end{pmatrix}, \tag{24}$$

the flux I (Eq. (22)) can be written as:

$$\begin{aligned}I&=\int_{\partial C_A\cap\tau}\alpha\left[a(\xi,\eta)\left(-\frac{\partial y}{\partial\xi}d\xi-\frac{\partial y}{\partial\eta}d\eta\right)+b(\xi,\eta)\left(\frac{\partial x}{\partial\xi}d\xi+\frac{\partial x}{\partial\eta}d\eta\right)\right]\\ &=\int_{mOm'}\alpha\left[\left(b(\xi,\eta)\frac{\partial x}{\partial\xi}-a(\xi,\eta)\frac{\partial y}{\partial\xi}\right)d\xi+\left(b(\xi,\eta)\frac{\partial x}{\partial\eta}-a(\xi,\eta)\frac{\partial y}{\partial\eta}\right)d\eta\right]\\ &=\int_{-1}^{0}\alpha\left(b(\xi,0)\frac{\partial x}{\partial\xi}(\xi,\eta)-a(\xi,0)\frac{\partial y}{\partial\xi}(\xi,\eta)\right)d\xi+\int_{0}^{-1}\alpha\left(b(0,\eta)\frac{\partial x}{\partial\eta}(\xi,\eta)-a(0,\eta)\frac{\partial y}{\partial\eta}(\xi,\eta)\right)d\eta\\ &=\int_{-1}^{0}f(\xi,0)\,d\xi+\int_{0}^{-1}g(0,\eta)\,d\eta.\end{aligned} \tag{25}$$

Once $a(\xi,\eta)$ and $b(\xi,\eta)$ are expressed analytically, the integral I can be computed using a Gauss integration with two points for the integrals for f and g. One finds [36] that the integral I is finally equivalent to:

$$I=\int_{\partial C_A\cap\tau}\alpha\nabla T\cdot n\,dl=\alpha\left[\frac{1}{2}(\nabla T_M+\nabla T_G)\cdot n_{MG}+\frac{1}{2}(\nabla T_G+\nabla T_{M'})\cdot n_{GM'}\right]. \tag{26}$$

This discretisation is consistent on meshes composed of regular parallelograms [36]. The truncation error remains of order $O(h^2)$ on all other kinds of elements. On regular parallelograms, the scheme is monotonic if the elements are not too sheared and have a low aspect-ratio: the ratio between the element length and width must be lower than $\sqrt{3}$ and the minimum angle in the parallelogram ζ must satisfy $0\leqslant\cos(\zeta)\leqslant 0.5$. This point is clearly a drawback for using this finite-element

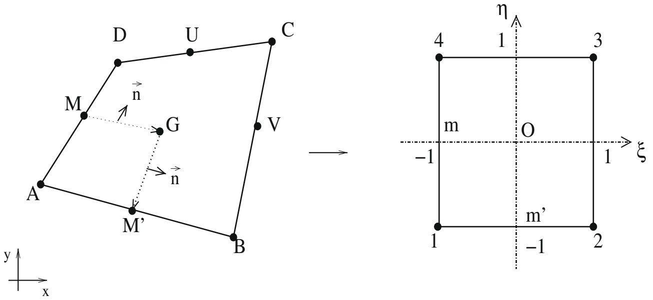

Fig. 6. Definition of the quadrilateral in classical coordinates and in iso-parametric ones. The arrow on the dual cell boundary of the left figure shows the integration direction and its normal unit vector n.

discretisation for high Reynolds number boundary layers where the element aspect-ratio can exceed 10^4. Moreover, for a hexahedron the computation of the diffusive flux on $\partial C_A \cap \tau$ requires the inversion of seven 3×3 Jacobian matrices. The numerical cost is therefore too large for practical applications.

In the following, this method will be denoted “EXact Finite-Element” approach (EXFE) as opposed to the “APproximated Finite-Element” method (APFE) presented in the following section.

5.6. Approximated finite-element reconstruction approach

It is the local and accurate evaluation of the gradient at the interface which bestows the good numerical properties to the EXFE method. Hence we seek a new method that uses locally varying gradients in the element, but gradients that are much less expensive and more robust to evaluate.

An obvious approach to nodal gradient computation is to use Green–Gauss integration over the primal mesh which has already been analysed by Coirier and Jorgenson [38]. Using the “centroidal path”, an integration path over the forming nodes of both elements containing the interface leads to a rotated Laplacian with decoupled face neighbours, which gives rise to a checker-board instability and is inconsistent for meshes with strongly varying mesh size (stretching). This approach has been adopted by Khawaja et al. [25] and can lead to acceptable results, but Coirier demonstrates its robustness problems. As an alternative, one could reconstruct face gradients from a linear variation of the nodal gradients computed for the MUSCL scheme, equivalent to Coirier’s “existing faces co-volume” approach. This approach leads to a non-compact stencil with decoupling of all immediate neighbours, resulting in a large number of spurious undamped modes. Using the “diamond” path where auxiliary state averages are computed at the barycentres leads to an inconsistent method on stretched meshes.

As an alternative approach to Green–Gauss integration, Papin’s tessellation method calculates local facet gradients on “third elements” formed within the primal elements. However, the computation of a gradient for each facet does not offer any savings over the EXFE method and the tessellation can produce poor quality third elements on high aspect-ratio grids or can fail on non-convex elements.

As a novel approach, let us propose to evaluate nodal gradients in each element on a “third element” formed from the edges joined at that node. In the case of simplex elements this recovers the P^1 gradients of the EXFE formulation. In the case of primitive elements except one case this results in the third element being a simplex of all edges joining at that node. The exception case is the apex node of a pyramid where four edges join: in this case Green–Gauss integration over the pyramid seems appropriate. Note that the quality of these third elements centred at the nodes maintains the quality of the primal element and does not degrade under aspect-ratio as Papin’s tessellation does. As a further approximation let us consider to base-facet gradients the average of the two nodal gradients at either end of the edge that the facet is attached to.

As an example, the gradient computation for node A for the two-dimensional quadrilateral in Fig. 6 would be based on the triangle ABD and equivalently for the other nodes.

The diffusion flux I (Eq. (22)) is then computed from:

$$I = \alpha \frac{\nabla T_D + \nabla T_A}{2} \cdot n_{MG} + \alpha \frac{\nabla T_A + \nabla T_B}{2} \cdot n_{GM'}. \tag{27}$$

A Taylor analysis shows that this scheme is conservative, and consistent on meshes composed of regular parallelograms. The truncation error remains of order $O(h^2)$ on all other kinds of elements, as for the EXFE method. On the other hand, the discretisation is monotonic on rectangles whatever their aspect-ratio.

5.7. Numerical experiments

The steady numerical solution is compared with the analytic solution for a pure heat diffusion problem on the square $[0,L] \times [0,L]$:

$$\int_{C_i} \frac{\partial T}{\partial t} \, dS = \int_{\partial C_i} \alpha \nabla T \cdot n \, dl, \tag{28}$$

with the constant diffusion coefficient α. In the following, $\alpha = 0.75$ has been used. Explicit time marching is used and local time steps are chosen according to stability restrictions for the heat equation. Dirichlet conditions are considered on the boundaries:

$$T_B(x,y) = \begin{cases} 0 & \forall x \in [0,L] \text{ and } y = 0, \\ \sin\left(\pi \frac{x}{L}\right) & \forall x \in [0,L] \text{ and } y = L, \\ 0 & \forall y \in [0,L] \text{ and } x = 0, \\ \sin\left(\pi \frac{y}{L}\right) & \forall y \in [0,L] \text{ and } x = L. \end{cases} \tag{29}$$

The exact stationary solution of the problem is:

$$u^{ex}(x,y) = \frac{1}{\sinh \pi} \left[\sinh\left(\pi \frac{x}{L}\right) \sin\left(\pi \frac{y}{L}\right) + \sinh\left(\pi \frac{y}{L}\right) \sin\left(\pi \frac{x}{L}\right) \right], \tag{30}$$

and is shown on Fig. 7.

The numerical error between exact and approximated solutions is measured in the L_2 norm using the following discrete expression:

$$\varepsilon = \left[\sum_{i=1}^{N_C} V_i \left(u_i^{ex} - u_i^{st} \right)^2 \right]^{1/2}, \tag{31}$$

where u_i^{ex} is the exact solution value at node i, u_i^{st} the numerical solution value at node i, V_i the dual cell volume. Assuming a general error distribution ε such that $\varepsilon = O(h^p)$, where h is the element diameter, p is the order of accuracy of a chosen method on a sequence of refined meshes composed of the same kinds of elements. In practice, p is deduced from mesh convergence analysis of numerical results by:

$$\log(\varepsilon) = p\log(h) + C, \tag{32}$$

with C a constant.

The four proposed methods will be denoted with the acronyms defined in Table 1. On triangles, methods EXFE, APFE and CV reduce to the classical P^1 finite-element method and hence are denoted P^1 in these cases.

Four kinds of meshes are considered and are associated with acronyms defined in Table 2.

A view of the different kinds of meshes considered is shown on Fig. 8. The irregular perturbed meshes are obtained from the square-based one through the random process:

$$\begin{cases} x_{pert} = x_{sq} + \frac{h}{c} d_1, \\ y_{pert} = y_{sq} + \frac{h}{c} d_2, \end{cases} \tag{33}$$

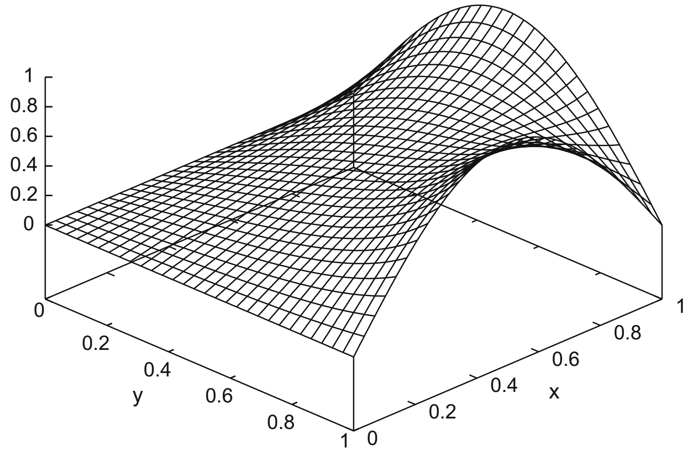

Fig. 7. Representation of the exact solution of the pure diffusion problem defined by Eqs. (28) and (29).

Table 1
Acronyms for the considered methods.

Acronym	Method for the gradient computation
EB	Edge-based method defined in Section 5.3
CV	Cell-vertex method defined in Section 5.4
EXFE	Exact finite-element method defined in Section 5.5
APFE	Approximated finite-element method defined in Section 5.6
P1	Classical P^1 finite-element method on triangles

Table 2
Acronyms for the considered meshes.

Acronym	Mesh
SQ	Mesh composed of regular squares
RE	Mesh composed of rectangles (two aspects ratio)
IQ	Mesh composed of irregular quadrilaterals
TR	Mesh composed of Delaunay-like triangles

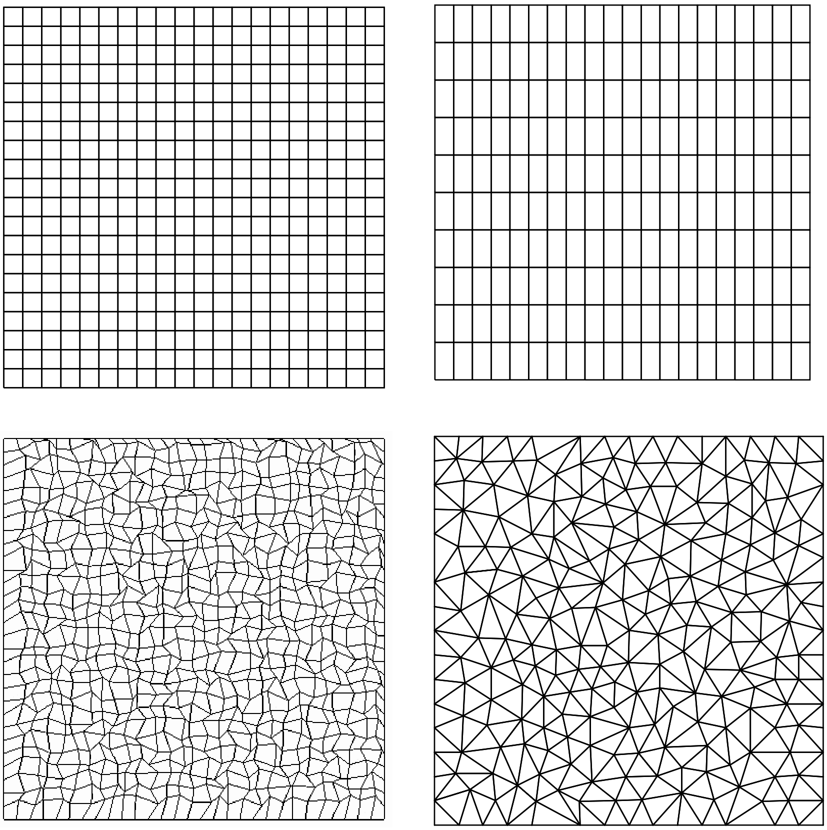

Fig. 8. Examples of meshes SQ, RE, TR and IQ, clockwise from top left.

where x_{sq} and y_{sq} are coordinates of the square-based mesh. d_1 and d_2 are random numbers defined in $[0,1]$, h is the element diameter and C is a coefficient chosen in order to have no reversed cells.

For each kind of mesh, three meshes are generated with three different element diameters. The pure diffusion test-case of Eq. (28) is solved with each of the four methods CV, EB, EXFE and APFE on all the meshes.

Fig. 9 presents the evolution of the logarithm of the error versus the logarithm of the element diameter for the different meshes, except for squares on which all discretisations are second-order accurate. The orders of accuracy obtained with the different discretisations are summarised in Table 3. In order to show the impact of the parameter δ_c for the CV method, two values are chosen. For method CVf, $\delta_c = 0.1$ is fixed while for method CVv, δ_c is the mean between maximum and minimum values of the stability interval (Eq. (20)).

The CV and APFE methods lose accuracy on perturbed quadrilateral meshes, but remain second-order accurate on triangular meshes. It can be observed that the accuracy of the EB method is particularly affected on the irregular quadrilaterals and triangular meshes. The EXFE method remains second-order accurate for meshes composed of triangles, of irregular quadrilaterals and of squares.

On rectangular meshes, high aspect ratios of 2 and 10 are tested. As for squares, the order of accuracy is about 2 for the CV methods, whatever the choice of the parameter δ_c (Eq. (18)). This is quite surprising for $\delta_c = 0.1$ which may not be in the stability interval of the CV method. The EB, APFE and EXFE methods are second-order accurate whatever the value of the aspect-ratio.

5.8. Linear preservation

Three methods arise as of most interest for the discretisation of viscous fluxes, namely the EXFE, APFE and EB methods. The CV methods will not be considered due to the lack of conservation. Here we test whether they are able to preserve an exact linear solution on a test-case suggested by Breil and Maire [39].

On the unit square $[0,1] \times [0,1]$, the heat equation with a constant diffusion coefficient equation (28) is solved with the following set of boundary conditions:

$$\begin{cases} T(x,y) = \begin{cases} 0 & \forall x \in [0,1] \text{ and } y = 0, \\ 0 & \forall x \in [0,1] \text{ and } y = 1, \end{cases} \\ \frac{\partial T}{\partial y} = \begin{cases} 0 & \forall y \in [0,1] \text{ and } x = 0, \\ 0 & \forall y \in [0,1] \text{ and } x = 1. \end{cases} \end{cases} \tag{34}$$

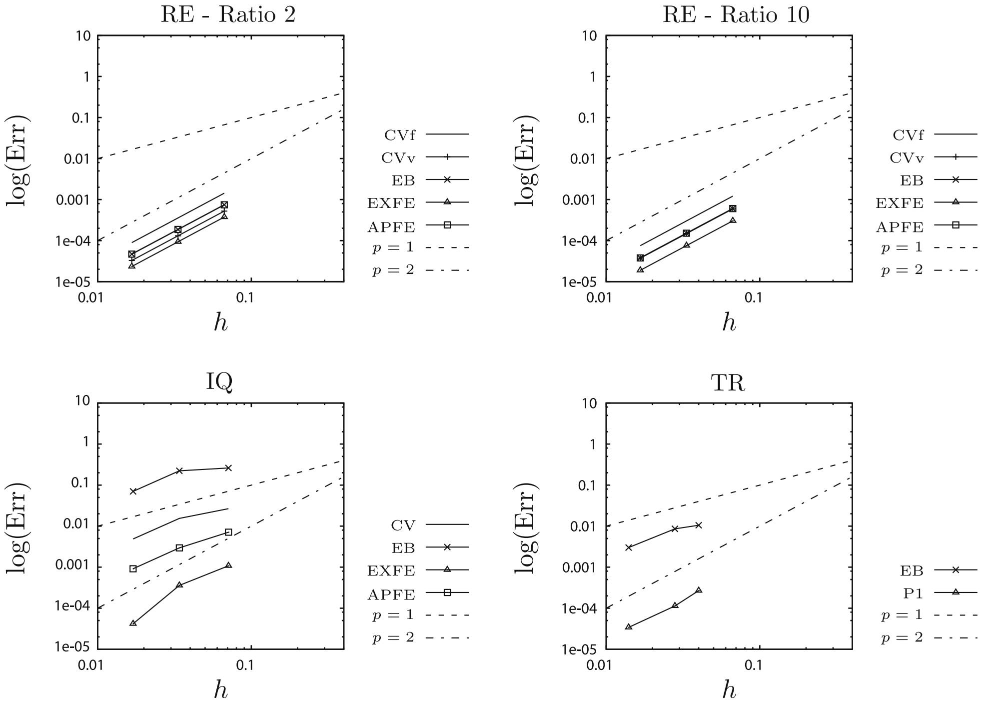

Fig. 9. Order p of convergence of the considered methods. On triangles, methods CV, APFE and EXFE are exactly the classical P^1 finite-element formulation.

Table 3
Order of accuracy according to mesh element types.

Element	CV		EB	EXFE	APFE
Square	2.01		2.01	2.00	1.98
Quadrilateral	1.18		0.92	2.27	1.44
Triangle	1.96		1.19	1.96	1.96
	$\delta_c = 0.1$	$\delta_c = f(h)$			
Rect., $r = 2$	2.00	1.998	1.999	2.001	1.998
Rect., $r = 10$	2.00	1.998	1.998	2.001	1.998

With the diffusion coefficient $\alpha = 1$, an exact analytical solution of Eq. (28), Eq. (34) is $T_{ex}(x, y) = x$.

Three meshes with square elements are considered based on a uniform discretisation in the x and y directions with 11, 21 and 41 nodes in each direction, resulting in diameters h of 0.1, 0.5 and 0.025.

Defining x_{sq} and y_{sq} as the coordinates of the nodes of a square-based mesh, a perturbed mesh is obtained with a smooth distortion using the following transformation:

$$\begin{cases} x_{pert} = x_{sq} + a_0 \sin(2\pi x_{sq}) \sin(2\pi y_{sq}), \\ y_{pert} = y_{sq} + a_0 \sin(2\pi x_{sq}) \sin(2\pi y_{sq}), \end{cases} \tag{35}$$

with the distortion parameter a_0. In the computations $a_0 = 0.1$ was used.

A perturbed mesh with an irregular distortion obtained through a random process is also considered. The transformation is the same as in Section 5.7, Eq. (33). Examples of square-based and perturbed meshes are shown in Fig. 10.

On the square-based meshes, the EXFE, APFE and EB methods reproduce the exact linear solution $T_{ex}(x, y) = x$. On the distorted meshes, the EXFE and APFE methods also reproduce the exact linear solution as shown in Fig. 11.

However, this is not the case for the EB method. As an example, an iso-line of the exact solution is compared with the same iso-line of the EB computation on Fig. 12.

Based on the L_2 norm of the error between the exact solution and the numerical one (Eq. (31)), the order of accuracy is about 1.9 on smoothly distorted meshes and reduces to about 1 on irregularly distorted meshes (Fig. 13). The correction added to the EB method for stability in the edge direction works well when the mesh and the diffusion direction are aligned. For the perturbed mesh, however, the correction induces a perturbation in the solution and a reduction in accuracy which depends on mesh quality.

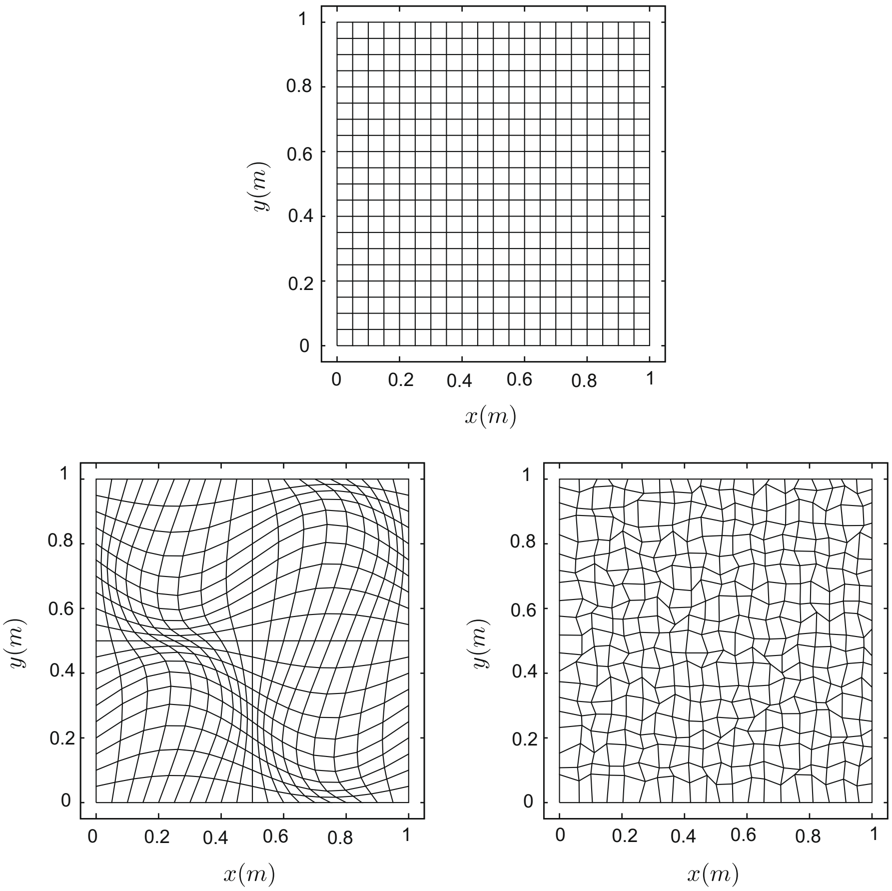

Fig. 10. Initial mesh composed of squares (up) and distorted ones obtained with Eq. (35) (bottom left) and Eq. (33) (bottom right). All meshes have 21 points in directions *x* and *y*.

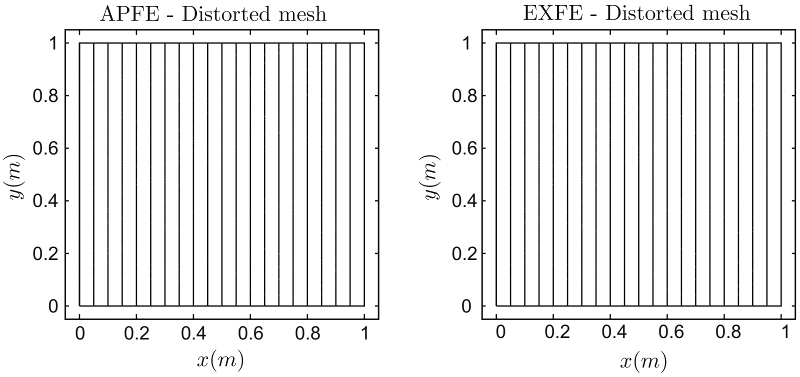

Fig. 11. Numerical solutions with APFE method on mesh composed of 20 × 20 distorted quadrilaterals (Eq. (35)) and with EXFE method on mesh composed of 20 × 20 distorted quadrilaterals (Eq. (33)).

Moreover, the numerical simulations show that the EB method allows the highest values of the CFL-like number, close to the maximum theoretical value for the linear heat equation of 0.5. Simulations with the EXFE approach require lowering the CFL-like number to 0.1 for the finest deformed mesh and 0.3 for the medium deformed mesh. The large values of CFL for the EB method may be explained by the high numerical diffusion of the scheme. For EXFE, the low CFL numbers are associated with the lack of monotonocity. Simulations with APFE method needs CFL-like numbers between those for EB and EXFE approaches.

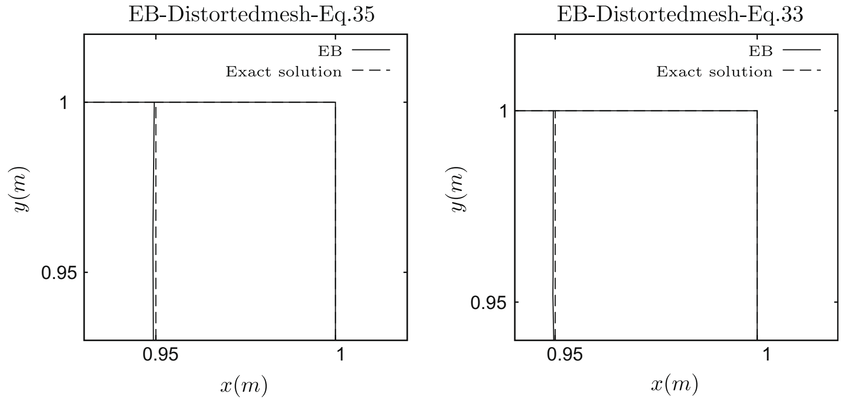

Fig. 12. Comparison of an iso-line of the temperature obtained with EB method and the same iso-line obtained with the exact solution on two meshes composed of 20 × 20 distorted quadrilaterals.

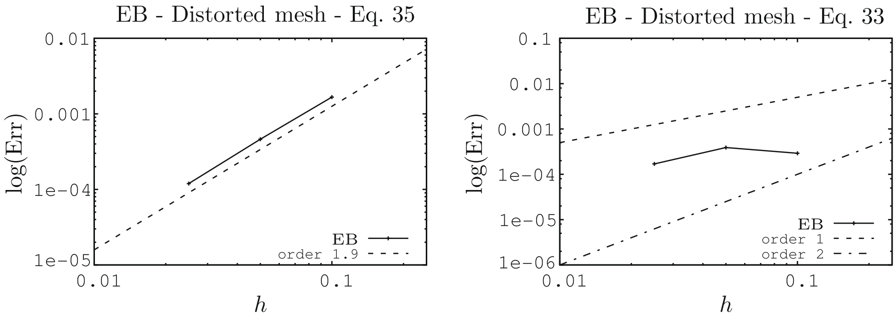

Fig. 13. Order p of convergence for the EB method on the distorted meshes.

5.9. Summary of the results for the heat equation

The results for the heat equation do not advise clearly against using a CV discretisation of the viscous fluxes: second-order of accuracy is obtained on smooth meshes composed of quadrilaterals. The lack of conservation is the main drawback of the method and it is the reason why the CV approach will not be considered in the following.

The EB method is very sensitive to grid irregularity. This may be a disadvantage on meshes from unstructured quadrilateral/hexahedral mesh generators with irregular elements and meshes produced with prismatic layers at the boundary extruded from surface triangulations. The method will perform well on regular structured grids which are aligned with the shear layers.

The best methods for the heat equation are the finite-element-based EXFE and APFE methods. The APFE method appears most suitable as it is only moderately less accurate on distorted quadrilaterals than EXFE method, but maintains full accuracy on high aspect-ratio elements. Both the EXFE and APFE methods are linear preserving on perturbed meshes where the EB method incurs a loss of accuracy.

6. Numerical results for the Navier–Stokes equations

After a short introduction to the base solver NSC2KE, the linearisation of the diffusion in the Navier–Stokes equations is discussed. Numerical results are presented for the flow over a laminar adiabatic flat plate and for the transonic turbulent flow over the RAE2822 airfoil.

6.1. NSC2KE solver

NSC2KE [9] is an unstructured vertex-based solver developed at INRIA (French National Agency for Research in Computer Science and Automation) and is freely available on the web [40]. NSC2KE uses a coupled finite-volume/finite-element technique to discretise convection and diffusion.

6.2. Non-linear diffusion

The diffusion coefficient in the RANS equations is not constant and a linearisation needs to be defined. Let us consider the two-dimensional configuration presented in Fig. 14 with the rectangle ABCD with barycentre G. M', V, U and M refer to the midpoints of segments [*AB*], [*BC*], [*CD*] and [*DA*], respectively. To simplify the explanations, expressions will be given for the temperature gradient ∇T.

For a laminar computation with the EXFE scheme one has to compute the integral *I*:

$$I = \int_{[MG]} \lambda \nabla T n \, ds + \int_{[GM']} \lambda \nabla T n \, ds, \tag{36}$$

where [*MG*] and [*GM*′] represent the facets of the dual cell C_A on the rectangle *ABCD*. The computation of Eq. (36) is based on a trapezoidal rule which guarantees second-order accuracy in the computation of the integral. This means that *I* is computed from:

$$I = \frac{\lambda_M + \lambda_G}{2} \frac{\nabla T_M + \nabla T_G}{2} n_{[MG]} + \frac{\lambda_G + \lambda_{M'}}{2} \frac{\nabla T_G + \nabla T_{M'}}{2} n_{[GM']}, \tag{37}$$

where *n* is the area-scaled facet normal. This linearisation is applied similarly to the other discretisations.

Alternative linearisations which interpolate the diffusion flux directly are possible and should be preferred in cases with strong gradients in the diffusion coefficients, in particular the formulation of Lörcher et al. [41] is based on the exact solution of a generalised diffusive Riemann problem. However, in order to demonstrate that the presented methods can be used in general existing finite-volume codes, we have conducted our numerical experiments with the formulation (Eq. (37)).

6.3. *Laminar flat plate simulations*

All computations with NSC2KE use the same parameters:

- a four-step Runge–Kutta explicit time stepping [9],
- local time steps account for convection and diffusion limits for stability,
- Roe's approximated Riemann solver [5],
- CFL number fixed at 0.5,
- inflow and outflow boundary conditions based on Steger–Warming flux splitting, as presented in [9].

6.3.1. *Numerical and physical parameters*

Laminar flow above an adiabatic wall is computed with NSC2KE. The flat plate is 1 m long, the inflow Mach number is $M_\infty = 0.8$ and the Reynolds number is $Re_\infty = 3 \times 10^4$. Four meshes are considered and are defined in Table 4. The mesh nodes are uniformly spaced in the tangential direction and a geometric law is applied in the direction normal to the plate. Table 4 lists the following properties of the meshes in the experiment:

- the distance between the first node above the wall and the wall, denoted *h*,
- the stretching *R* of successive cell heights,
- the number of nodes in the direction normal to the plate which fixes the domain height.

Each mesh has a triangular variant obtained by tessellation of the corresponding quadrilateral mesh. Meshes 3 based on rectangles and triangles are shown on Fig. 15.

6.3.2. *Effect of diffusion schemes for rectangle-based meshes*

In Fig. 16, the pressure and the friction coefficients distributions at the wall are shown for mesh 1 and mesh 4. Mesh 1 is not sufficiently refined to capture the compression near the leading edge, resulting in low values of C_p and an under-estimation of the friction coefficient C_f. All methods lead to very similar results. Good agreement is found between the theoretical law of Blasius for the friction coefficient and the numerical values for C_f. Similar results are obtained for meshes 2, 3 and 4 (results for meshes 2 and 3 are not presented).

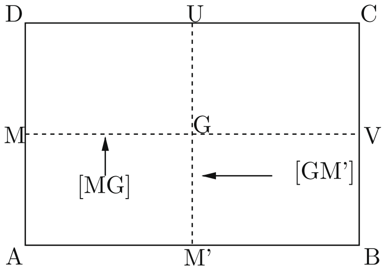

Fig. 14. Notations introduced for the non-linear diffusion explanations.

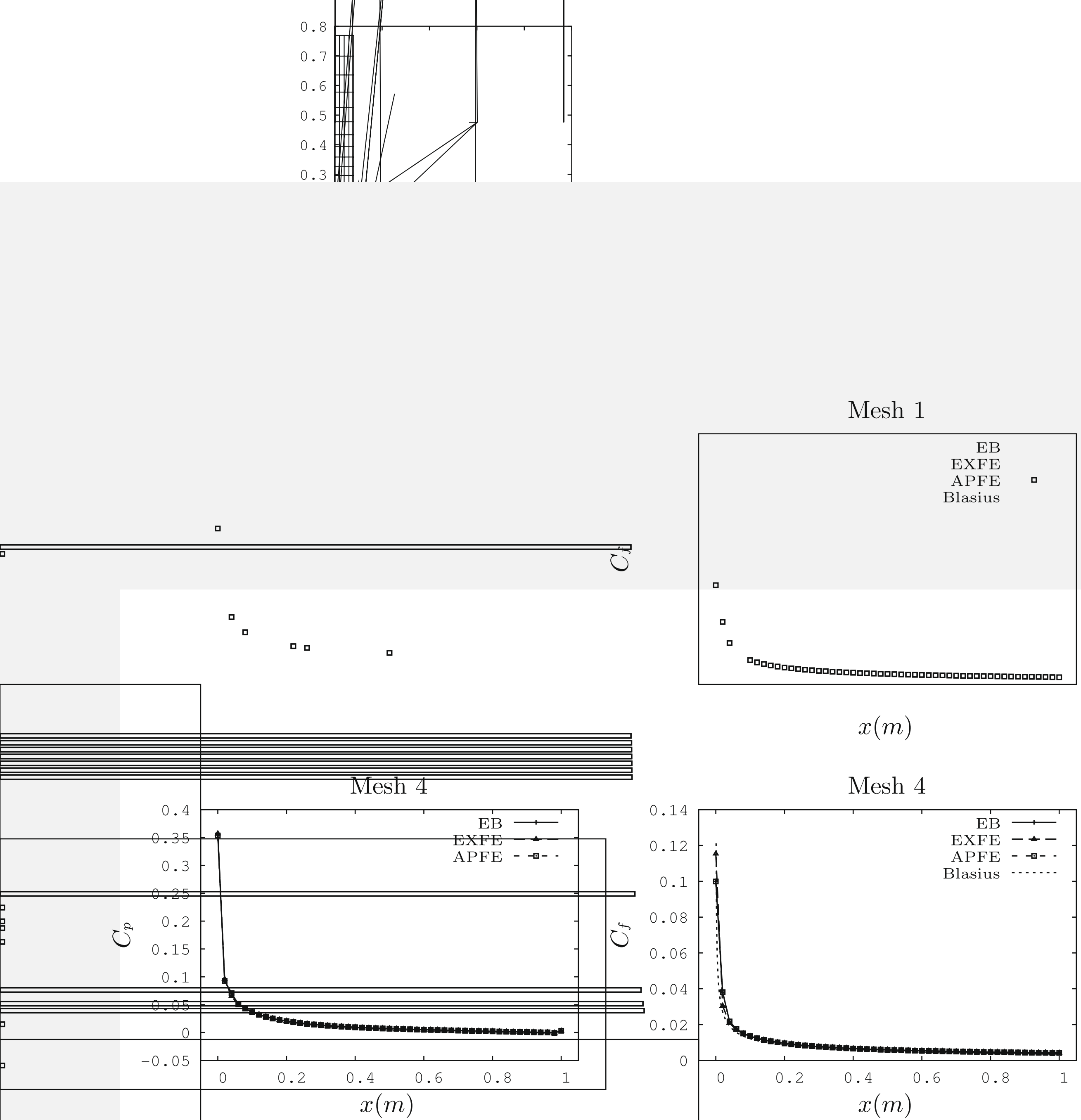

Fig. 16. Wall pressure and skin friction coefficients distribution obtained on meshes 1 and 4 composed of rectangles (second-order accuracy for the convection scheme).

6.3.5. Conclusions on the flat plate results

For the laminar flat plate only small differences can be observed in friction or wall-pressure coefficients between the classical P^1 finite-element method applied on triangles and the studied methods for rectangles. The EB, APFE and EXFE schemes exhibit good numerical properties for the laminar flat plate case. Rectangle-based meshes result in a gain in accuracy and an appreciable reduction in CPU time and number of iterations.

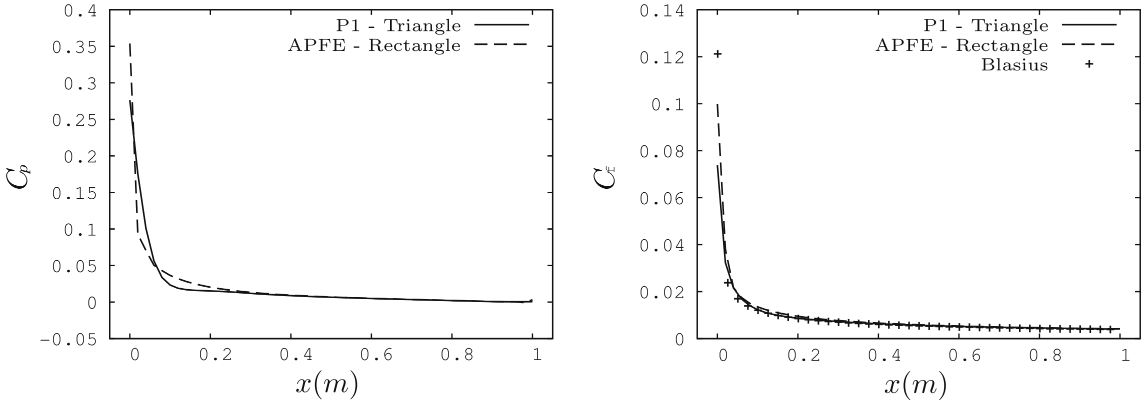

Fig. 19. Comparison of pressure coefficient obtained on triangle and rectangle mesh. Second-order accuracy for the convection scheme, mesh 4.

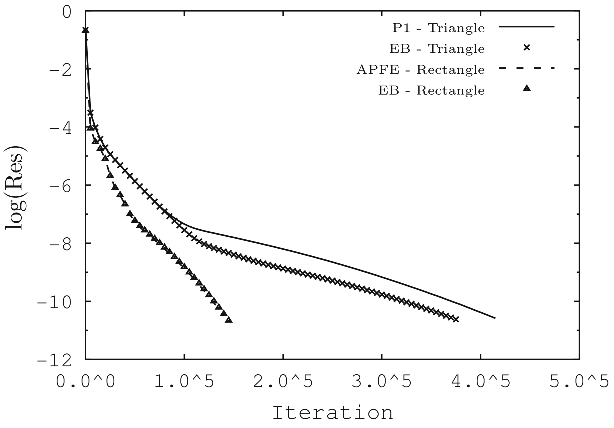

Fig. 20. Comparison of convergence obtained on the triangle and rectangle meshes with second-order accuracy.

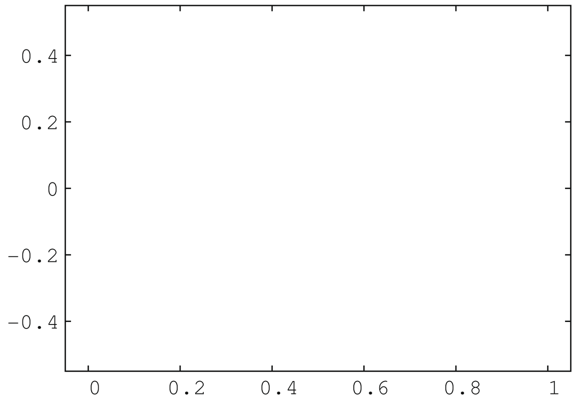

6.4. Turbulent flow around the RAE2822 airfoil

The turbulent transonic flow over a RAE2822 profile is a well-documented test-case for which there are experimental data for the wall-pressure and skin-friction coefficients. The considered test-case is referenced as test-case 9 in [42]. The flow is fully attached to the adiabatic wall boundary and inflow variables are $M_\infty = 0.734$, $Re_\infty = 6.5 \times 10^6$ for a normalised chord

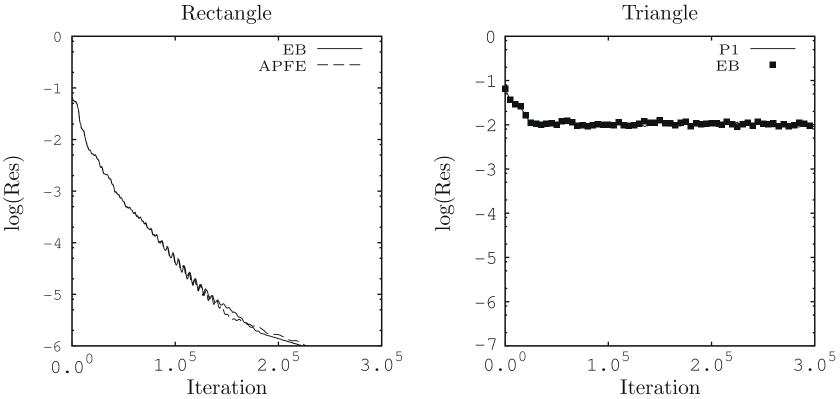

Fig. 22. RAE2822: convergence residuals on rectangle and triangle meshes.

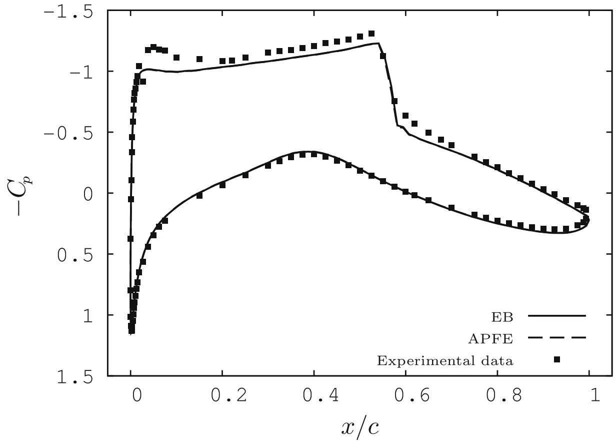

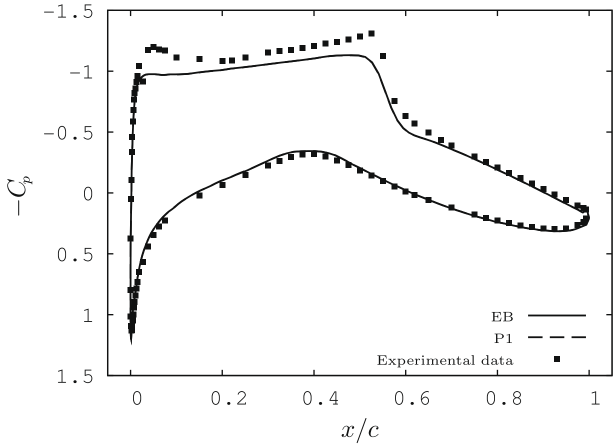

Fig. 23. RAE2822: pressure coefficient distribution on the wing for rectangle-based mesh (up) and triangle-based mesh (down).

7. Conclusion

Four different approaches to model the diffusive fluxes on hybrid meshes have been studied and compared. The first one is based on a cell-vertex approximation (CV), the second one on an edge-based approach (EB) and the two last ones on finite-element reconstruction of the gradient (APFE and EXFE methods). The theoretical analysis of local consistence and monotonicity reveals that the methods based on a finite-element-like gradient reconstruction exhibit the best properties, which is confirmed by the numerical experiments with the linear heat equation. The cell-vertex method needs a corrective term to be monotonic which makes the formulation non-conservative. The edge-based method is second-order accurate on regular isotropic parallelograms, but only of order one on irregular and on high aspect-ratio meshes.

The methods based on finite-element reconstruction are consistent on meshes composed of regular parallelograms and their truncation error is of order $O(h^2)$. These methods reduce to the classical P^1 finite-element formulation on triangles and tetrahedra, which is desirable for the extension of simplex solvers as their behaviour on simplex meshes remains unaltered.

The exact (EXFE) and approximated finite-element (APFE) methods however perform differently on high aspect-ratio meshes. The EXFE method is monotonic on parallelograms with a ratio between the length and width below $\sqrt{3}$ and the angle of the parallelogram ζ bounded as $0 \leqslant \cos(\zeta) \leqslant 0.5$. The APFE method is monotonic on any regular mesh and maintains second-order accuracy on high aspect-ratio rectangles.

The exact and approximated finite-element approaches (APFE, EXFE) are the only methods which can recover exactly the linear solution on a smoothly distorted isotropic mesh, while the order of accuracy for the edge-based (EB) method drops below second-order.

The conservative methods EB, APFE and EXFE have been implemented in the Navier–Stokes solver NSC2KE and results have been obtained for the RANS equations coupled with a two-layer k–ε turbulence model using an aligned regular grid. The use of a mesh composed of rectangles leads to an increase of the precision of gradient-based quantities such as wall friction. On the high aspect-ratio quadrilateral mesh, the exact finite-element (EXFE) approach fails to converge due to a lack of monotonicity. The boundary layer is computed with similar accuracy by both the approximated finite-element and edge-based methods and with similar convergence rates. This is certainly due to the strong alignment of the flow and the mesh. This result may not hold for shear layers that are oblique to the mesh as often arise in detached flows or for hybrid meshes with less regularity in the shear layers.

References

[1] T. Barth, Aspects of unstructured grids and finite-volume solvers for the Euler and Navier–Stokes equations, in: VKI Lecture Series 1994-05, Von Kármán Institute, Rhode-St.-Genèse, Belgium, 1995.
[2] P. Roe, The influence of mesh quality on solution accuracy, in: 19th VKI Lecture Series on Computational Fluid Dynamics 1989-04, Von Kármán Institute, Rhode-St.-Genèse, Belgium, 1989.
[3] A. Dervieux, Steady Euler simulations using unstructured meshes, in: 16th VKI Lecture Series on Computational Fluid Dynamics 1985-04, Von Kármán Institute, Rhode-St.-Genèse, Belgium, 1985.
[4] P. Rostand, B. Stoufflet, Finite volume Galerkin methods for viscous gas dynamics, Tech. Rep. RR-863, INRIA (1988).
[5] P.L. Roe, Approximate Riemann solvers, parameter vectors and difference schemes, Journal of Computational Physics 43 (2) (1981) 357–372.
[6] A. Dervieux, Steady Euler simulations using unstructured meshes, in: J. Geymonat (Ed.), Partial differential Equations of hyperbolic type and Applications, World Scientific, 1987, pp. 34–112 (Ch. 2).
[7] B. Stoufflet, J. Periaux, F. Fezoui, A. Dervieux, 3D hypersonic Euler numerical simulations around space vehicles usinf adapted finite elements, in: 25th Aerospace Sciences Meeting and Exhibit, AIAA Paper 86-0560, 1986.
[8] F. Fezoui, B. Stoufflet, A class of implicit upwind schemes for Euler simulations with unstructured meshes, Journal of Computational Physics 84 (1) (1989) 174–206.
[9] B. Mohammadi, Fluid dynamics computation with NSC2KE. An user-guide. Release 1.0., Tech. Rep. RT-0164, INRIA (1994).
[10] R. Eymard, T. Gallouët, R. Herbin, Finite volume methods, in: P. Ciarlet, J. Lions (Eds.), Handbook of Numerical Analysis, vol. VII, North Holland, 2000, pp. 713–1020.
[11] V. Billey, J. Periaux, B. Stoufflet, A. Dervieux, L. Fezoui, V. Selmin, Recent improvements in Galerkin and upwind Euler solvers and application to 3D transonic flow in aircraft design, Computer Methods in Applied Mechanics and Engineering 75 (1–3) (1989) 409–414.
[12] D.J. Mavriplis, V. Venkatakrishnan, A unified multigrid solver for the Navier–Stokes equations on mixed element meshes, International Journal of Computational Fluid Dynamics 8 (4) (1997) 247–263.
[13] P. Moinier, J. Müller, M. Giles, Edge-based multigrid schemes and preconditioning for hybrid grids, AIAA Journal 40 (10) (2002) 1954–1960.
[14] A. Haselbacher, J. McGuirk, G. Page, Finite volume discretization aspects for viscous flows on mixed unstructured grids, AIAA Journal 37 (2) (1999) 177–184.
[15] M. Galle, Unstructured viscous flow solution using adaptive hybrid grids, ICASE/LaRC workshop on adaptive grid methods, NASA Langley Research Center (1995).
[16] P. Crumpton, P. Moinier, M. Giles, An unstructured algorithm for high Reynolds number flows on highly stretched grids, in: C. Taylor, J.T. Cross (Eds.), Numerical Methods in Laminar and Turbulent Flow, Pineridge Press, 1997, pp. 561–572.
[17] R. Eymard, T. Gallouët, R. Herbin, Finite volume approximation of elliptic problems and convergence of an approximate gradient, Applied Numerical Mathematics 37 (2001) 31–53.
[18] P. Crumpton, J. Mackenzie, K. Morton, Cell vertex algorithms for the compressible Navier–Stokes equations, Journal of Computational Physics 109 (1) (1993) 1–15.
[19] O. Colin, A finite element operator for diffusion terms in AVBP, Tech. Rep., Institut Français du Pétrole (2003).
[20] CERFACS CFD Team, The AVBP handbook, Tech. Rep., CERFACS (2007).
[21] D. Pan, J. Cheng, Upwind finite-volume Navier–Stokes computation on unstructured triangular meshes, AIAA Journal 31 (9) (1993) 1618–1625.
[22] L. Flandrin, P. Charrier, B. Dubroca, A robust finite-volume method for computations of two-dimensional unstructured hybrid meshes, in: S. Wagner, E.H. Hirschel, J. Priaux, R. Riva (Eds.), Computational Fluid Dynamics'94, Wiley, New York, 1994, pp. 301–308.
[23] J. Coirier, An adaptatively-refined, cartesian, cell-based scheme for the Euler and Navier–Stokes equations, Tech. Rep. TM-106754, NASA (1994).
[24] K. Lipnikov, D. Svyatskiy, Y. Vassilevski, Interpolation-free monotone finite volume method for diffusion equations on polygonal meshes, Journal of Computational Physics 228 (3) (2009) 703–716.

[25] A. Khawaja, Y. Kallinderis, V. Parthasarathy, Implementation of adaptive hybrid grids for 3D turbulent flows, in: AIAA, 34th Aerospace Sciences Meeting and Exhibit, AIAA Paper 96-0026, Reno, January 1996.

[26] O. Peroomian, S. Chakravarthy, U. Goldberg, A 'grid-transparent' methodology for CFD, in: AIAA, 35th Aerospace Sciences Meeting and Exhibit, AIAA Paper 97-0724, Reno, January 1997.

[27] M. Papin, Contribution à la modélisation d'écoulements hypersoniques particulaires. Etude et validation d'un modèle diphasique discret., Ph.D. Thesis, Université de Sciences et Technologies de Bordeaux 1 (2005).

[28] W. Reed, T. Hill, Triangular mesh methods for the neutron transport equation, Tech. Rep. LA-UR-73-479, Los Alamos Scientific Laboratory (1973).

[29] J. Nitsche, Über ein Variationsprinzip zur Lösung von Dirichlet-Problemem bei Verwendung von Teilräumen, die keinen Ransbedingungen unterworfen sind, in: Abhandlungen aus dem mathematischen Seminar der Unisertität Hamburg, No. 36, 1971, pp. 200–212.

[30] B. Cockburn, C. Shu, Tvb Runge–Kutta local projection discontinuous Galerkin finite element method for conservation laws. II: General framework, Mathematics of Computation 52 (186) (1989) 411–435.

[31] B. van Leer, Towards the ultimate conservative difference scheme. V. A second-order sequel to Godunov's method, Journal of Computational Physics 32 (1) (1979) 101–136.

[32] D. Arnold, F. Brezzi, B. Cockburn, L. Marini, Unified analysis of discontinuous Galerkin methods for elliptic problems, SIAM Journal of Numerical Analysis 39 (5) (2002) 1749–1779.

[33] M. Zhang, C. Shu, An analysis of three different formulations of the discontinuous Galerkin method for diffusion equations, Mathematical Models and Methods in Applied Sciences 13 (3) (2003) 395–413.

[34] B. van Leer, S. Nomura, Discontinuous Galerkin for diffusion, in: 17th AIAA Computational Fluid Dynamics Conference, AIAA Paper 2005-5108, 2005.

[35] G. Gassner, F. Lörcher, C. Munz, A contribution to the construction of diffusion fluxes for finite volume and discontinuous Galerkin schemes, Journal of Computational Physics 224 (2) (2007) 1049–1063.

[36] V. Auffray, Étude comparative de schémas numériques pour la modélisation de phénomènes diffusifs sur maillages hybrides, Ph.D. Thesis, Institut National Polytechnique de Toulouse (2007).

[37] T. Schönfeld, M. Rudgyard, Steady and unsteady flows simulations using the hybrid flow solver AVBP, AIAA Journal 37 (11) (1999) 1378–1385.

[38] J. Coirier, C.P. Jorgenson, A mixed volume grid approach for the Euler and Navier–Stokes equations, in: AIAA, 34th Aerospace Sciences Meeting and Exhibit, Reno, AIAA Paper 96-0762, January 1996.

[39] J. Breil, P.-H. Maire, A cell-centered diffusion scheme on two-dimensional unstructured meshes, Journal of Computational Physics 224 (2) (2007) 785–823.

[40] Source files of NSC2KE. <http://pauillac.inria.fr/cdrom/www/nsc2ke/eng.htm>.

[41] F. Lörcher, G. Gassner, C. Munz, An explicit discontinuous Galerkin scheme with local time-stepping for general unsteady diffusion equations, Journal of Computational Physics 227 (11) (2008) 5649–5670.

[42] T. Hellström, L. Davidson, A. Rizzi, Reynolds stress transport modelling of transonic flow around the RAE2822 airfoil, in: AIAA, 32nd Aerospace Sciences Meeting, Reno, AIAA Paper 94-0309, January 1994.

[43] An European initiative on validation of CFD-codes, in: W. Haase, F. Brandsma, E. Elsholtz, M. Leschziner, D. Schwamborn (Eds.), Notes on Numerical Fluid Mechanics, Vieweg Verlag, 1993.

[44] B. Mohammadi, Complex turbulent flows computation with a two-layer approach, International Journal for Numerical Methods in Fluids 15 (7) (1992) 747–771.